

Numerical investigation of liquid and supercritical CO₂ flow behaviors through 3D self-affine rough fractures

Jiawei Li^{a*}, Zi Li^a, Wanju Yuan^b, Ximing Lei^a, Sergio Andres Galindo Torres^c, Claudia Cherubini^d, Alexander Scheuermann^a, Ling Li^e

^{a*} School of Civil Engineering, University of Queensland, Brisbane 4072, Australia

^b Faculty of Engineering and Applied Science, University of Regina, Regina S4S 0A2, Canada

^c Department of Civil Engineering and Industrial Design, University of Liverpool, Liverpool L69 3BX, United Kingdom

^d Department of Physics and Earth Sciences, University of Ferrara, via Saragat 1 - 44122 Ferrara, Italy

^e School of Engineering, Westlake University, Hangzhou 310024, China

Abstract

In recent years, CO₂ has been utilized to be injected into natural and induced fracture reservoirs with the purpose of enhanced natural energy resources recovery. In this study, the influence of liquid and supercritical CO₂ properties under different pressure and temperature conditions on flow behaviors through a 3D self-affine fracture with rough surfaces is investigated with the application of Lattice Boltzmann method (LBM). CO₂ has properties highly dependent on pressure and temperature and this study focuses on the liquid and supercritical CO₂ properties because it is very common for CO₂ to maintain liquid and supercritical states in deep reservoirs. LBM was used to simulate liquid and supercritical CO₂ flow through a single fracture with rough surfaces. In addition to CO₂ properties, the effects of pressure differences between the injecting and discharging surfaces of the fracture were also considered. The density and dynamic viscosity of CO₂ display similar trends in responses to changes in pressure and temperature. Simulation results show that the average velocity of CO₂ flow changes considerably with temperatures and pressures. The streamlines distributions revealed the changes of tortuosity under different temperature and pressure conditions, which follows a similar trend to that of the average velocity. A detailed analysis of the effects of the temperature, pressure and upscaling velocity on tortuosity was conducted based on the relevant curves and streamlines distributions. It was found that the values of tortuosity have a close relationship with the kinematic viscosity, which depends on temperature and pressure conditions.

Keywords

CO₂ properties; rough fracture surfaces; tortuosity; streamlines

Introduction

The technologies for carbon capture, utilization and storage (CCUS) have been developed and implemented to reduce CO₂ emissions in the last decades [1-3]. There are several CO₂ utilization methods that have been applied in energy areas with taking CO₂ storage in the reservoirs into consideration, including CO₂ flooding, liquid CO₂ fracturing, enhanced geothermal systems (EGS) and methane displacement from gas hydrates [4-10]. In addition, the supercritical temperature and pressure for CO₂ is 31.04 °C and 7.38 MPa, which means it is easy for CO₂ to keep its liquid and supercritical states under reservoir conditions (oil, gas

43 and geothermal) [11-13]. Therefore, the understanding of liquid and supercritical CO₂ through
44 a fracture has a great significance for modelling CO₂ flow efficiently and accurately in natural
45 and induced fractured reservoirs.

46 In recent years, many studies have mainly focused on investigating the fracture propagation
47 process and flow in the fracture networks of liquid and supercritical CO₂ as fracturing liquids
48 through field testing, laboratory experiments and simulations [14-19]. The leak off properties
49 of liquid CO₂ fracturing are presented based on field and laboratory measurements [20]. The
50 growth behaviours of fractures induced by supercritical CO₂ in tight sandstones were explored
51 through a series of experiments under triaxial stress conditions [21]. The effects of water and
52 supercritical CO₂ on fracture propagation behaviours were compared, indicating that
53 supercritical CO₂ creates shorter fractures in comparison with water under similar injection
54 conditions [22]. And CO₂ has been used to improve geophysical identification and
55 characterization of fractures and faults in push-pull well tests at enhanced geothermal system
56 sites [23]. In addition, with taking CO₂ properties into consideration, a phase state control
57 model was developed to simulate supercritical CO₂ fracturing under different temperatures [24].
58 As for mathematical model of the fluid flow through a fracture, the Parallel Plate theory for the
59 characterization of fractures has been the most popular method due to its convenience for
60 quantitative analysis [25-28]. However, the complex roughness of natural fracture surfaces
61 under reservoir conditions is ignored. In order to gain a better characterization of fluid flow
62 into a fracture, it is of critical importance to investigate the effects of rough surfaces of the
63 fracture. Though the fracture roughness is very complex, some experimental methods, such as
64 X-ray computed tomography, have been proposed to characterize fracture roughness efficiently
65 [29-31]. Different experiments of water flow through a single fracture have been designed to
66 examine the effects of fracture surface roughness, apertures and Reynolds number [32-38]. The
67 experimental investigations of water flow paths through natural rough fractures with the
68 application of tracer have been presented [39]. Combined with the experiments under confining
69 pressure, the aperture distributions and fluid flow through a single rough fracture are
70 characterized [40]. In addition to the experiments, mathematical methods and theories have
71 been developed to the modelling of fluid flow through a fracture more accurately. A more
72 accurate solution corresponding to the Navier-Stokes equations was introduced to describe
73 fluid flow between slightly rough surfaces of real fractures [41]. The classical Local Cubic Law
74 with considering the fact that various values of fracture apertures are distributed in spatial
75 locations was proposed [42]. The use of various simplifications and applied ranges of Reynolds
76 Lubrication equation for fluid flow into a fracture were discussed and evaluated [43, 44]. A
77 model that incorporates surface geometry of natural fractures has been upgraded with the purpose
78 of channelling flow evaluation [45]. And a modified Local Cubic Law that a low range of local
79 Reynolds Numbers can be applied was developed, which also integrates fracture surface
80 roughness and local tortuosity [46].

81 The Lattice Boltzmann method has been applied for mathematical model and simulation of
82 fluid flow through a fracture with rough surfaces in the 21st century [47, 48]. It is shown that
83 fracture anisotropy has a greater effect on the fracture permeability compared with the mean
84 aperture and fractal dimension of the fracture by analysing the flow behaviours through a
85 fracture with rough surfaces on the basis of Lattice Boltzmann simulations [49]. The LBM was
86 also used to investigate the influence of wettability for different fluids on corresponding

87 interfacial areas in a rough fracture with self-affinity [50]. In addition, influences of main and
88 secondary roughness for fracture surfaces on nonlinear behaviours of water flow in 3D rough
89 fractures with the characteristic of self-affinity were analysed with the application of the LBM
90 [51]. Another study shows that with the increase of fracture roughness, the eddy volumes
91 become larger and the effective hydraulic conductivities decreases in rough fractures [52]. An
92 experiment has been designed for the investigation of water flow through fractures with rough
93 surfaces that are generated by 3D printing technology and then the experimental results are
94 compared with simulation results from LBM [53].

95 In recent years, investigations of liquid and supercritical CO₂ through a single rough fracture
96 are very limited, but several studies on heat transfer of water flow through rough fractures [54-
97 57]. The influences of supercritical CO₂ flow on the heat transfer and spatial distributions on
98 the rough fracture surface was studied with the finite volume method [19]. In this paper, the
99 effects of relevant factors, including liquid and supercritical CO₂ properties, fracture surface
100 roughness etc, on flow behaviors are presented and analysed when liquid and supercritical CO₂
101 flow into a rough fracture.

102 **Self-affine rough fracture surfaces**

103 In order to reflect the rough surfaces of natural fractures accurately, the fractal theory has been
104 applied to create the rough fracture surfaces with the characteristic of self-affinity artificially
105 [58-60]. The self-affinity is a characteristic of a fractal whose pieces can be scaled by different
106 amounts along X and Y directions, meaning that the self-similarity of these fractal objects can
107 be observed [61, 62]. And an anisotropic affine transformation should be used to rescale and
108 test the self-affinity [61].

109 The variance of the surface height is defined as follows [63]:

$$110 \quad \sigma^2(r) = \left\langle \left[Z(x+rh_x, y+rh_y) - Z(x, y) \right]^2 \right\rangle \quad (1)$$

111 where σ^2 represents the variance, r is a constant and Z is the surface height, h is the
112 increment of surface height along X and Y directions.

113 When Hurst exponent is used for fracture generation, its range is usually between 0 and 1. It
114 should be noticed that the values of Hurst exponent have been found to locate in the range of
115 0.45 and 0.85 in most cases [59, 64]. In addition, it has been mentioned that the fracture
116 roughness follows a self-affine distribution that is produced by the fractal dimension. Here the
117 fractal dimension D_f has the following relationship with the Hurst exponent [59]:

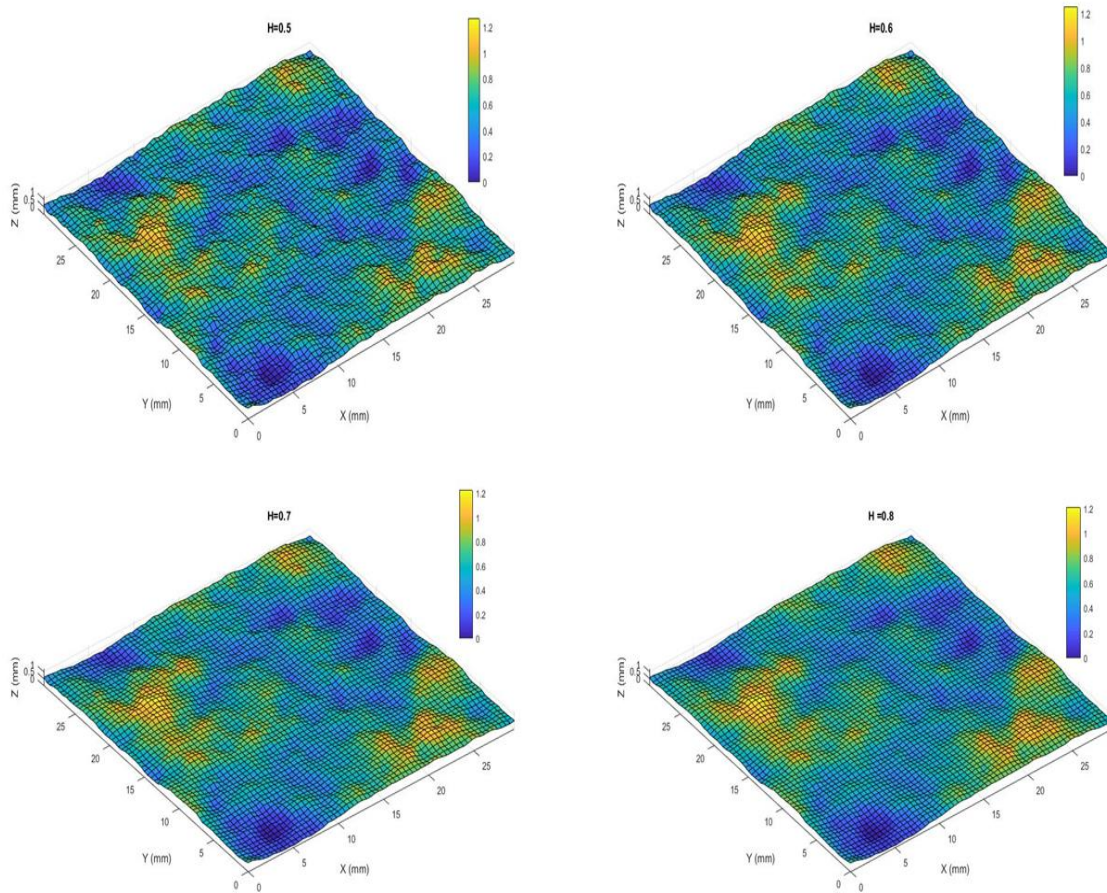
$$118 \quad D_f = 3 - H \quad (2)$$

119 Another important parameter, power spectral density ratio, is also used for the generation of
120 rough fracture surfaces, which considers the variation between the top and bottom fracture
121 surfaces [65, 66].

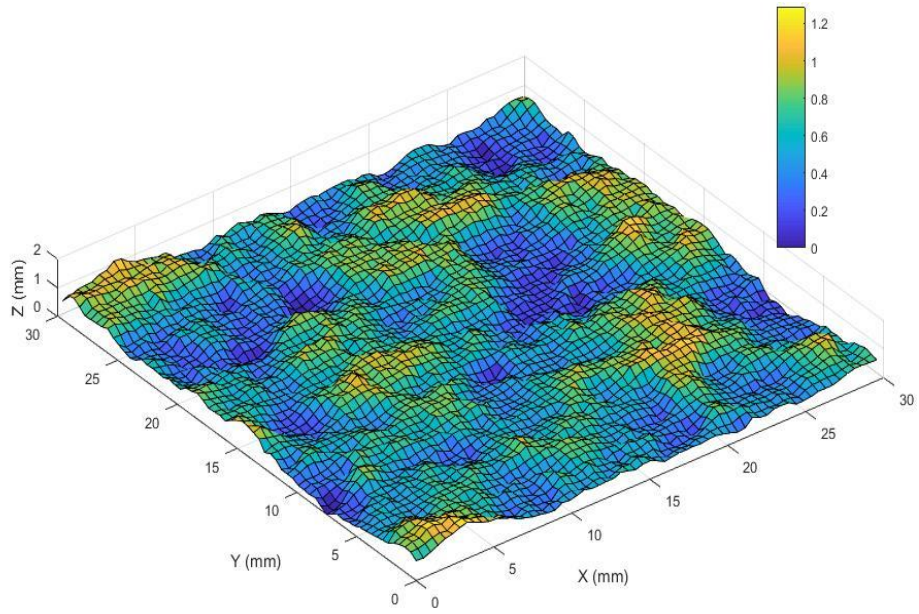
122 On the basis of the proposed theories, the self-affine fracture with rough surfaces have been
123 generated by using the 64×64 data sets from the software SynFrac [66]. And Matlab R2017a
124 has been used to deal with the data sets from SynFrac. The examples of self-affine fracture
125 surfaces corresponding to different values of Hurst exponents with remaining other variables
126 that affect fracture rough surfaces constant are shown in Fig. 1. The length and width of fracture
127 models are both 30 mm and there are grids distribution on the X-Y plane in order to reflect

128 64×64 data sets of heights that varies due to self-affine fracture roughness. As is shown in Fig.1
129 the heights follows a self-affine fractal distribution and the heights of several grids increase
130 with Hurst exponent increasing.

131 In this study, a schematic of apertures that is with $\sigma = 0.2$ mm for the generated fracture
132 surfaces with $H = 0.6$ shown in Fig. 2 will be used for further simulations. In Fig. 2, deeper
133 blue colors reflect the smaller apertures, up to zero, and larger values of apertures are
134 represented by brighter yellow colors, which will be combined with streamlines distributions
135 for analysis. The corresponding top and bottom surfaces are shown in Fig. 3. The statistical
136 histogram of apertures of a self-affine fracture with $\sigma = 0.2$ mm and $H = 0.6$ is shown in Fig.
137 4.

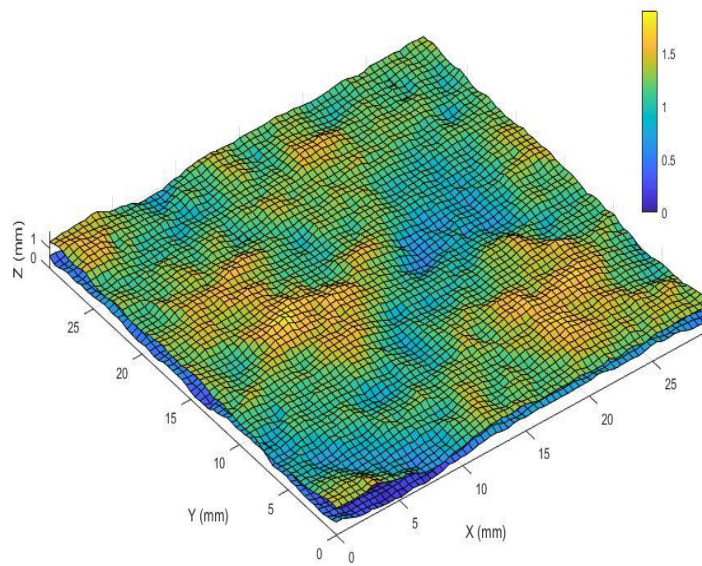


138
139 Fig. 1 Four self-affine fracture bottom surfaces corresponding to different Hurst exponents
140 with $\sigma = 0.2$ mm



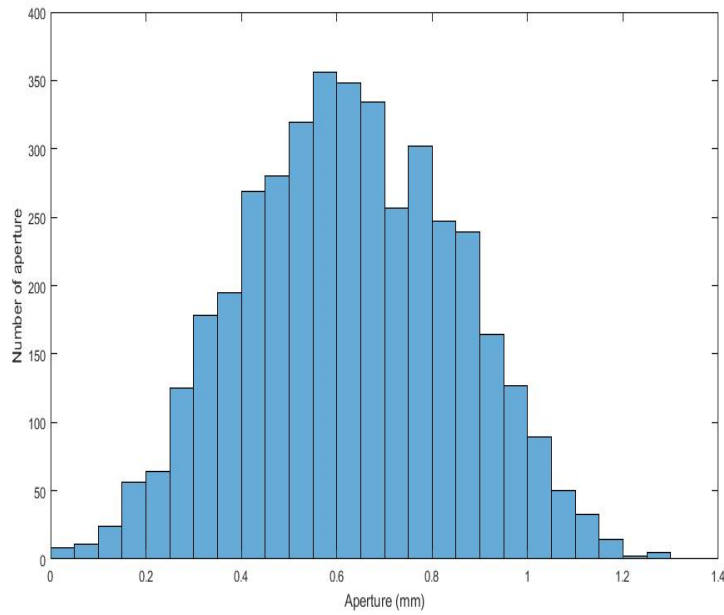
141
142
143

Fig. 2 A self-affine fracture aperture distributions with $\sigma = 0.2$ mm and $H = 0.6$



144
145
146

Fig.3 The top and bottom surfaces of the fracture with $\sigma = 0.2$ mm and $H = 0.6$



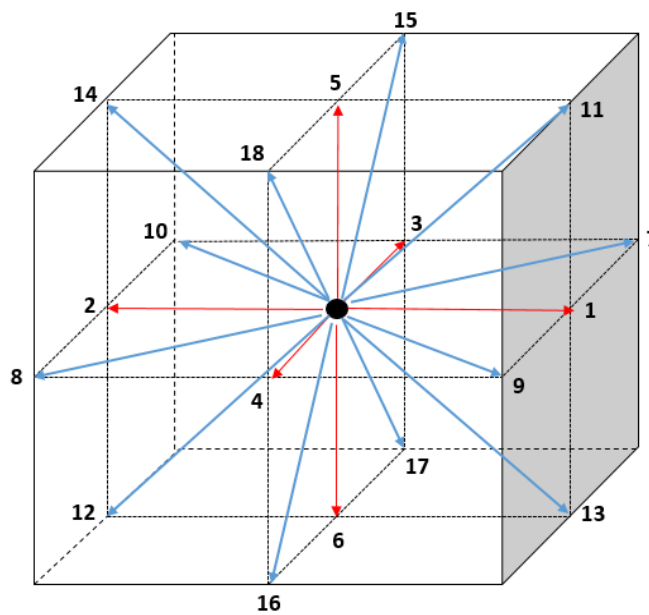
147

148 Fig.4 Statistical histogram of the apertures in a self-affine rough fracture with $\sigma = 0.2$ mm
 149 and $H = 0.6$

150 **Lattice Boltzmann Method (LBM)**

151 The LBM is a highly efficient method that simulates single and multiphase flow systems under
 152 the conditions of complex geometries, which has been applied in different areas, such as fluids
 153 flow through porous media and fractures, thermal fluids flow etc. [67-71]. In this paper, a
 154 D3Q19 model was used to simulate liquid and supercritical CO₂ through a single fracture
 155 model [72]. There are nineteen discrete velocities distributed in a cubic space shown in Fig. 5.

156



157

158 Fig. 5 D3Q19 model: velocity vectors in a cell

$$159 \quad \vec{e}_i = \begin{cases} 0, & i = 0, \\ (\pm 1, 0, 0), (0, \pm 1, 0), (0, 0, \pm 1), & i = 1 - 6, \\ (\pm 1, \pm 1, 0), (\pm 1, 0, \pm 1), (0, \pm 1, \pm 1) & i = 7 - 18. \end{cases} \quad (3)$$

160 The distribution function satisfying the evolution rule based on the Chapman-Enskog
161 expansion of the Boltzmann equation is shown as follows [73]:

$$162 \quad f_i(\vec{x} + \vec{e}_i \delta_t, t + \delta_t) = f_i(\vec{x}, t) + \Omega_{col} \quad (4)$$

163 where $f_i(\vec{x}, t)$ is the fluid particle distribution function with velocity \vec{e}_i (the mesoscopic
164 velocity in the i -th direction) at position \vec{x} and time t , δ_t is the length of time step and Ω_{col} is
165 the collision operator representing the relaxation process due to the collision of the fluid
166 particles.

167 The Bhatnagar-Gross-Krook model for the collision operator is applied here [68]:

$$168 \quad \Omega_{col} = \frac{\delta_t}{\tau} (f_i^{eq} - f_i) \quad (5)$$

169 where τ is the relaxation time and f_i^{eq} is the equilibrium distribution.

170 And the relaxation time τ is the parameter that governs the rate at which the fluid tends
171 towards equilibrium with the following expression [67]:

$$172 \quad \tau = \frac{3\nu\delta_t}{\delta_x^2} + 0.5 \quad (6)$$

173 where ν is the kinematic viscosity of fluid.

174 The f_i^{eq} is expressed as follows:

$$175 \quad f_i^{eq} = \omega_i \rho \left(1 + 3 \frac{\vec{e}_i \cdot \vec{u}}{C^2} + \frac{9(\vec{e}_i \cdot \vec{u})^2}{C^4} - \frac{3u^2}{2C^2} \right) \quad (7)$$

176 with $C = \delta_x / \delta_t$ defined as a characteristic lattice velocity in a cell size. The density ρ and the
177 velocity \vec{u} at a cell position \vec{x} can be calculated respectively as:

$$178 \quad \rho(\vec{x}) = \sum_{i=0}^{18} f_i(\vec{x}) \quad (8)$$

$$179 \quad \vec{u}(\vec{x}) = \frac{\sum_{i=0}^{18} f_i(\vec{x}) \vec{e}_i}{\rho(\vec{x})} \quad (9)$$

180 Similar to the D3Q15 model, the weight factors in the D3Q19 model are:

$$181 \quad \omega_i = \begin{cases} 1/3, & i = 0, \\ 1/18, & i = 1 - 6, \\ 1/36, & i = 7 - 18. \end{cases} \quad (10)$$

182 The relationship between pressure and density in LBM is defined as [67]:

$$183 \quad P = \frac{1}{3} C^2 \rho \quad (11)$$

184 Numerical Modelling

185 To evaluate the influence of liquid and supercritical CO₂ properties on flow behaviors through
186 a self-affine rough fracture, Equation of State is an efficient method to calculate relevant

187 properties, such as density and viscosity, under different temperatures and pressures. The
188 calculations of liquid and supercritical CO₂ properties have been realized by a commercial
189 software (WinProp, CMG) on the basis of Peng-Robinson Equation of State. It should be
190 noticed that the supercritical temperature and pressure for CO₂ is 31.04 °C and 7.38 MPa. Fig.
191 6 and 7 show the changes in density and dynamic viscosity of CO₂ with different pressures and
192 temperatures. It can be seen that there are four regions in both Fig. 6 and 7: gas, liquid, two-
193 phase and supercritical regions. The chosen temperature and pressure ranges should satisfy the
194 existence of liquid and supercritical CO₂. In this study, the temperature range corresponding to
195 CO₂ is between 20 and 100°C and the pressure is from 10 to 60 MPa. With the gravity effect
196 being also neglected. In addition, flow behaviours of CO₂ under certain temperature and
197 pressure has been investigated with a series of pressure gradients between the injecting and
198 discharging surfaces.

199 In order to gain a more realistic simulation of liquid and supercritical CO₂ flow through self-
200 affine rough fractures, the numerical fracture model should reflect the fracture geometries
201 accurately. The fracture model shown in Fig. 3 will be used for further numerical simulations.
202 Its length and width equal to 30 mm and its height is no more than 2 mm with the solid boundary
203 sealed on top and bottom surfaces. The fracture parameters including $\sigma = 0.2$ mm, $H = 0.6$ are
204 kept constant. Because the fracture model is built based on the 64×64 data sets, the 30 mm×30
205 mm X-Y plane can be divided into 256×256 grids. This means a resolution of 0.1171875 mm
206 in X, Y and Z directions are used for the fracture model, which takes both fracture surface
207 characterization and computational efficiency into consideration.

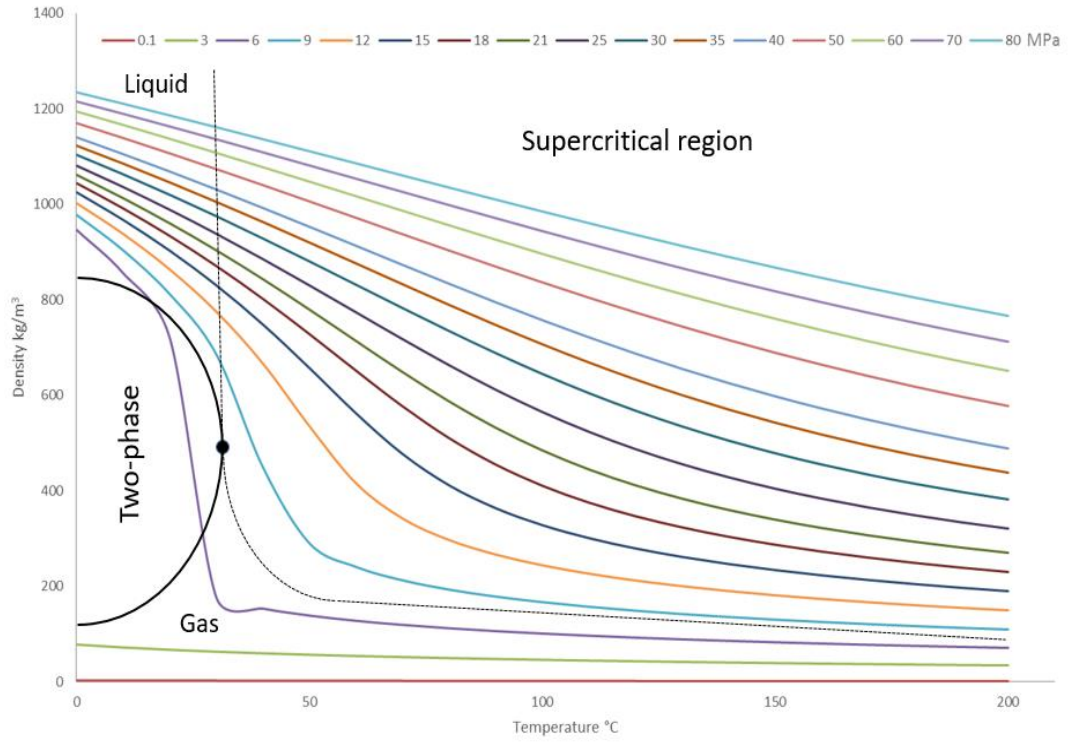
208 Fig. 8 shows the injecting and discharging surfaces of the fracture model in the Lattice
209 Boltzmann domain. As is shown in Fig. 8, the red color represents the solid rock and the blue
210 color illustrates fracture space between the top and bottom fracture surfaces. The lateral sides
211 of fracture model are set as periodic boundaries and the fracture model is assumed to be non-
212 deformable during the flowing process. Here periodic boundary condition is adopted to have a
213 better schematic of the fracture model. The simulation results calculated by the periodic and
214 solid boundary condition are compared for the validation of calculating accuracy. When the
215 pressure difference between the injecting and discharging surfaces equals to 0.01 Pa, the
216 average velocities for the solid boundary under the pressure condition 40 MPa and temperature
217 condition 20°C are 4.7227×10^{-6} m/s and the average velocity of the periodic boundary equals
218 to 4.97×10^{-6} m/s at the same conditions, with a relative difference of 4.97 %. The simulation
219 results of the solid boundary are a little smaller than those of the periodic boundary because
220 the initial velocities on the solid boundary equals to zero. In addition, a smaller resolution of
221 0.05859375 mm in X, Y and Z directions has been used to check the mesh independence. With
222 the same conditions, the average velocities for a smaller resolution is 5.189×10^{-6} m/s. The
223 comparisons show that the periodic boundary and resolution settings meet the simulation
224 requirements for the research goal in this study.

225 There are four different pressure differences between the injecting and discharging surfaces:
226 10, 1, 0.1 and 0.01 Pa that are used for the following simulations under different pressure and
227 temperature conditions in this study. The changes of CO₂ density caused by such small pressure
228 differences can be negligible directly, which means CO₂ densities under different pressure and
229 temperature conditions can be assumed to be constant. In addition, it should be noticed that

230 there are no phase transitions between liquid and supercritical CO₂ due to the same reasons.
 231 The heat transfer and spatial variations are also neglected with the temperature assumed to be
 232 constant because small scale of the fracture model and the pressure differences between the
 233 injecting and discharging surfaces are pretty small. As for transformation between real physical
 234 and lattice Boltzmann units, the following equations can be used with considering the fact that
 235 there are single liquid or supercritical CO₂ flow in the simulations [74]:

$$236 \quad \text{Re} = \frac{u_{real} L_{real}}{\nu_{real}} = \frac{u_{LBM} L_{LBM}}{\nu_{LBM}} \quad (12)$$

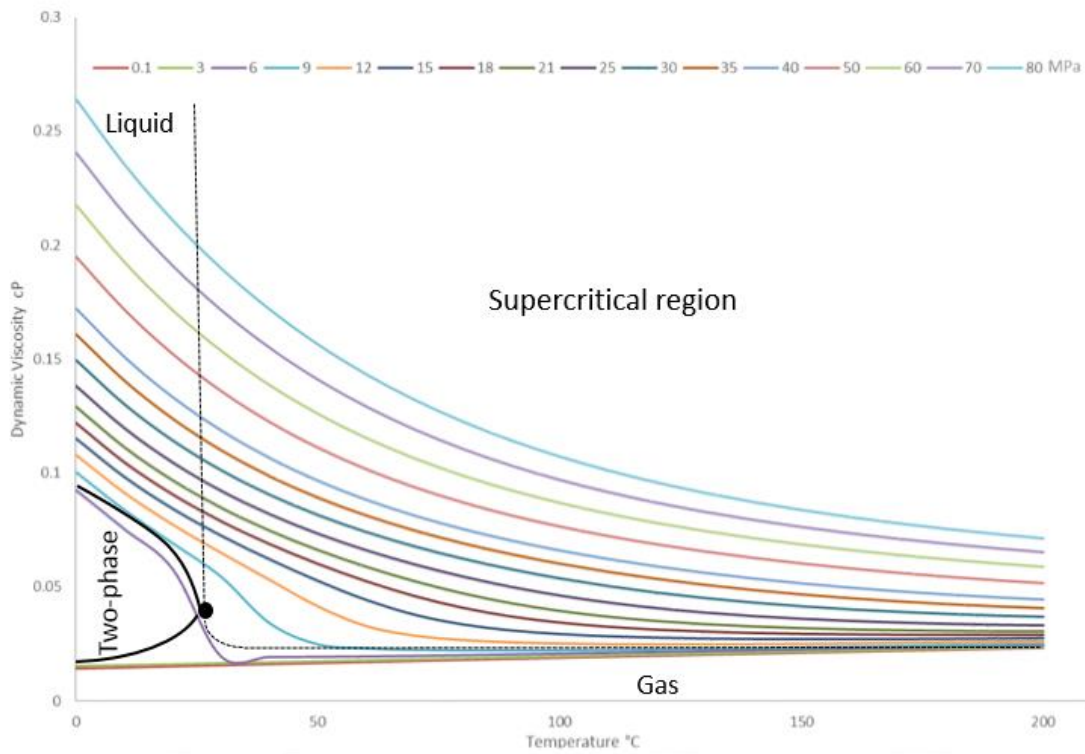
237 where Re is the Reynolds number, L is the characteristic length.
 238 Before the beginning of the simulation, there is no velocity distribution in the fracture. In the
 239 simulation, the CO₂ flow will reach a steady state after some time and the velocities at steady
 240 state will be used for further calculation and analysis. For example, Fig. 9 shows the velocity
 241 distributions for the time $t_a = 40000$ and $50000ts$ being the same in Lattice Boltzmann domain,
 242 which means the flow has reached the steady state. It can be seen that Fig. 8 and 9 strictly
 243 follow the fracture aperture distributions in Fig. 2. In Fig. 8, there is an area of fracture aperture
 244 that is pretty narrow on the injecting surface, which corresponds to fracture aperture
 245 distribution of the deepest blue color on the injecting surface in Fig. 2. In addition, there is a
 246 large blank area on velocity distributions in Fig. 9, which is located at about 14-20 mm in X
 247 direction and 16-22 mm in Y direction. In Fig. 2, this area on the X-Y plane has deep blue
 248 colors that means the apertures are very small and the flow prefers other flow paths with larger
 249 apertures. Three points a, b and c locating at 20.15625, 20.625 and 21.09375 mm at Y direction
 250 are used to generate the corresponding aperture and velocity distributions along X direction,
 251 which is shown in Fig. 10. The Location a, b and c all belongs to the range of the blank area
 252 mentioned above. In Fig. 10, it can be seen that the apertures from 14 to 16 mm along X
 253 direction are much smaller and the velocities equal to zero, which reflects the existence of the
 254 blank area in Fig. 9.



255

256

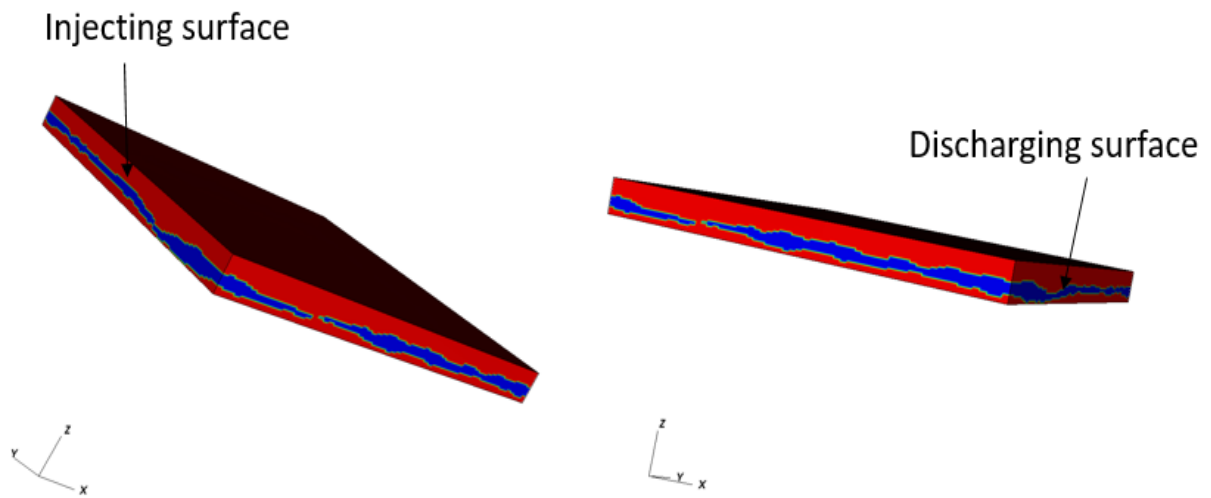
Fig. 6 CO₂ density corresponding to temperature and pressure



257

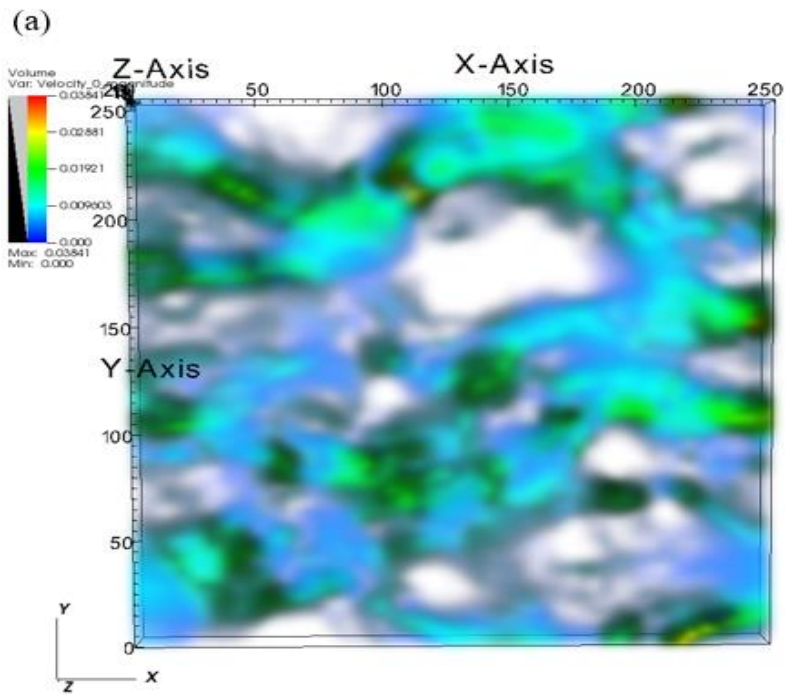
258

Fig. 7 CO₂ dynamic viscosity corresponding to temperature and pressure

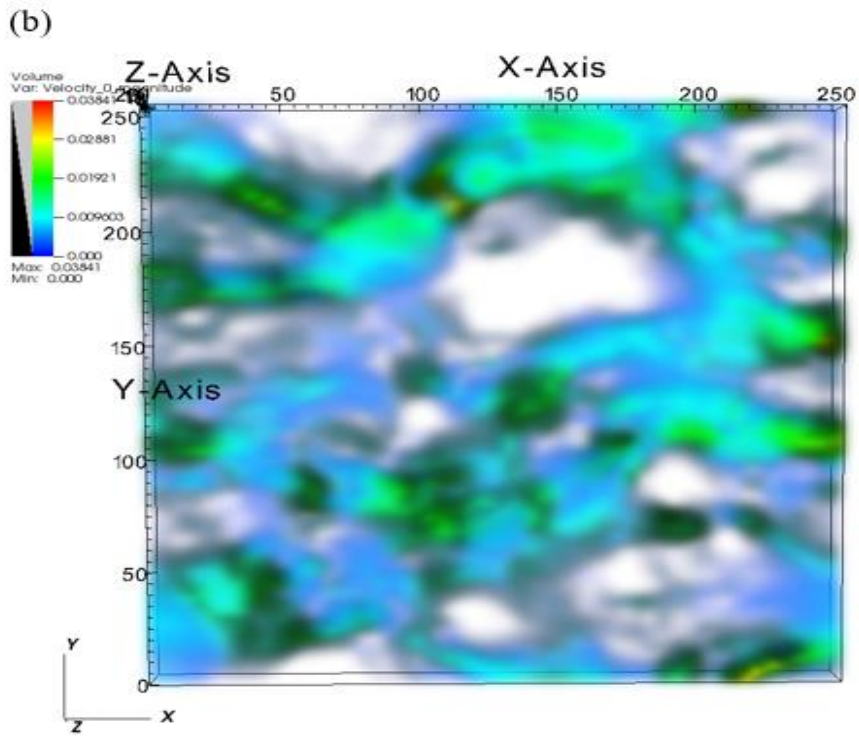


259
260
261

Fig. 8 Schematic of the self-affine rough fracture model from injecting and discharging surfaces



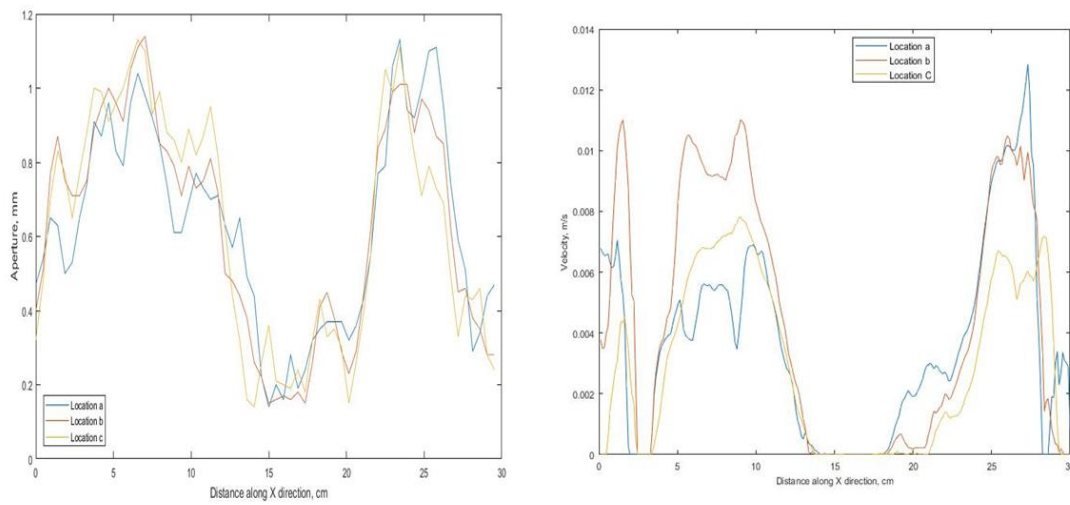
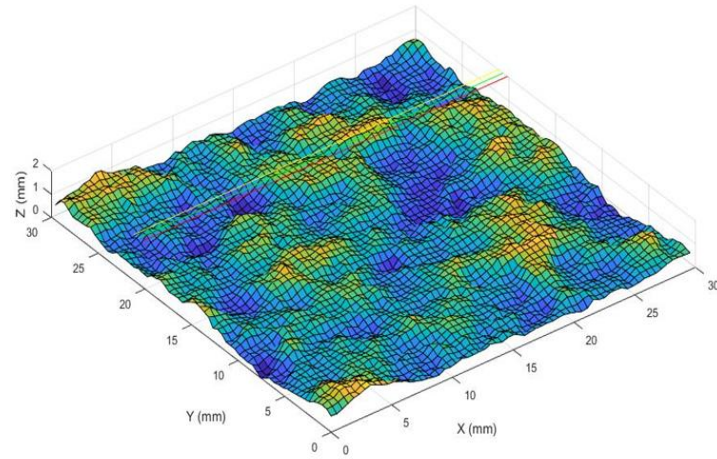
262
263



264

265

Fig. 9 Velocity distributions and magnitude for (a) $t_a = 40000ts$ and (b) $t_a = 50000ts$



266
267
268

Fig. 10 Aperture and velocity distributions along X direction for Transects a, b and c

269 **Results Analysis**

270 In Fig. 10, it is shown that the average velocity and tortuosity correspond to different pressure
271 conditions at the temperature of 20, 60 and 100 °C with the pressure difference between the
272 injecting and discharging surfaces (Δp) being 10 Pa. The tortuosity can be calculated based on
273 the following equation [75, 76]:

274
$$Tortuosity = \frac{\sum |V(x, y, z)|}{\sum |V_x(x, y, z)|} \quad (13)$$

275 where $|V_x(x, y, z)|$ is the magnitude of velocity in X direction that is the main flow direction
276 and $|V(x, y, z)|$ is the magnitude of velocity vector at a certain location with the coordinates of
277 (x, y, z) :

278
$$|V(x, y, z)| = \sqrt{V_x(x, y, z)^2 + V_y(x, y, z)^2 + V_z(x, y, z)^2} \quad (14)$$

279 The values of velocity can be gained directly from LBM simulations and then transformed into
280 the real physical units. It can be seen that, with corresponding to the kinematic viscosities, the

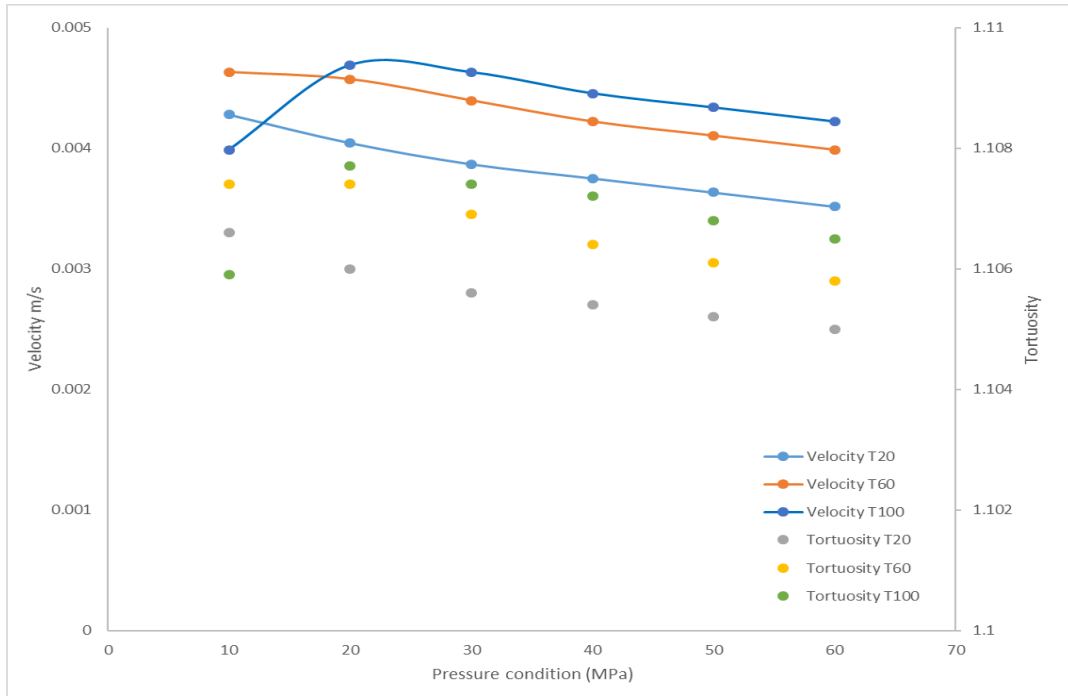
281 average velocity for the temperature conditions $T=20$ and 60°C both have gradually decreasing
282 trends with the increase of pressure conditions and the average velocity for $T=100^{\circ}\text{C}$ increases
283 initially and then decreases in Fig. 11. The kinematic viscosity refers to the ratio of dynamic
284 viscosity to density. For three temperature conditions, the values of the average velocity are
285 around 0.004 and 0.005 m/s. In addition, the average velocity values of $T=60^{\circ}\text{C}$ are always
286 larger than those of $T=20^{\circ}\text{C}$. However, the values for $T=100^{\circ}\text{C}$ show a sudden hump with the
287 changes of temperatures. The tortuosity has the same trend to the average velocity for each
288 temperature condition. The values of tortuosity locate in the range of 1.104 to 1.108. Fig. 12
289 shows the average velocity and tortuosity under the same pressure and temperature conditions
290 with $\Delta p = 0.01$ Pa. With the same changing trends, the values of the average velocity are much
291 smaller and the values of tortuosity for three temperature conditions become a little larger
292 compared with the results in Fig. 11. Fig. 11 and 12 show that the average velocity and
293 tortuosity of liquid and supercritical CO_2 for different pressure conditions change with
294 changing temperature.

295 Fig. 13 is an example of streamlines for two pressure conditions $P=10$ and 60 MPa with the
296 temperature condition $T=20$ and 100°C . Under these conditions, the CO_2 are at liquid and
297 supercritical state respectively. As it is known, tortuosity is the ratio of the length of a
298 streamline—a flow line or path—between two points to the straight-line distance between those
299 points. It should be noticed that velocity distributions in Fig. 9 and streamlines in Fig. 13 both
300 reflect the preferential flow paths of liquid and supercritical CO_2 flow through fracture rough
301 surfaces, which also represent CO_2 concentration on fracture rough surfaces because it can be
302 seen that there is no liquid and supercritical CO_2 flow on some areas on the fracture rough
303 surface based on simulation results. In Fig. 13, small differences of streamlines that reflect the
304 tortuosity between two cases are caused by the changes of pressure conditions. And it can be
305 found that the time for streamlines shaping varies when the pressure condition equals to 10 and
306 60 MPa from time legends next to the streamline distributions. The area that is surrounded by
307 red borders showing that the streamlines for $P=60$ MPa in this area become more tortuous than
308 those for $P=10$ MPa when the temperature equals to 20. As for $T=100^{\circ}\text{C}$, the comparison of
309 streamlines do not show obvious differences. In addition to direct observations from the
310 streamlines distributions, the tortuosity values of the area surrounded by red borders are
311 calculated and compared with the tortuosity values of the whole fracture. As for the tortuosity
312 calculations in the surrounded area, the grids from 60 to 90 along Y direction and from 175 to
313 225 along X direction are chosen. In this area, the values of tortuosity for the temperature 20
314 and 100°C under the pressure condition 10 MPa are 1.1754 and 1.1742 respectively and those
315 under the pressure condition 60 MPa are 1.1785 and 1.1755. And the differences of the
316 tortuosity values for the whole area of the fracture surfaces between 10 MPa and 60 MPa for
317 the temperature 20 and 100°C are 0.0016 and 0.0006. Table. 1 shows a direct comparison for
318 better understanding. So it is obvious that the differences of the tortuosity values between 10
319 MPa and 60 MPa in the surrounded area are much larger than those in the whole fracture, which
320 are reflected on the observed streamlines distributions. Based on the above analysis, the
321 tortuosity has a tight relationship with the pressure conditions with considering the average
322 velocities being similar.

323 Table. 1 Comparisons of tortuosity differences between the surrounded and whole areas at
324 different pressure conditions

	Tortuosity of P=10 MPa	Tortuosity of P=60 MPa	Tortuosity differences in the surrounded area	Tortuosity differences of the whole area
T=20°C	1.1754	1.1785	0.0031	0.0016
T=100°C	1.1742	1.1755	0.0013	0.0006

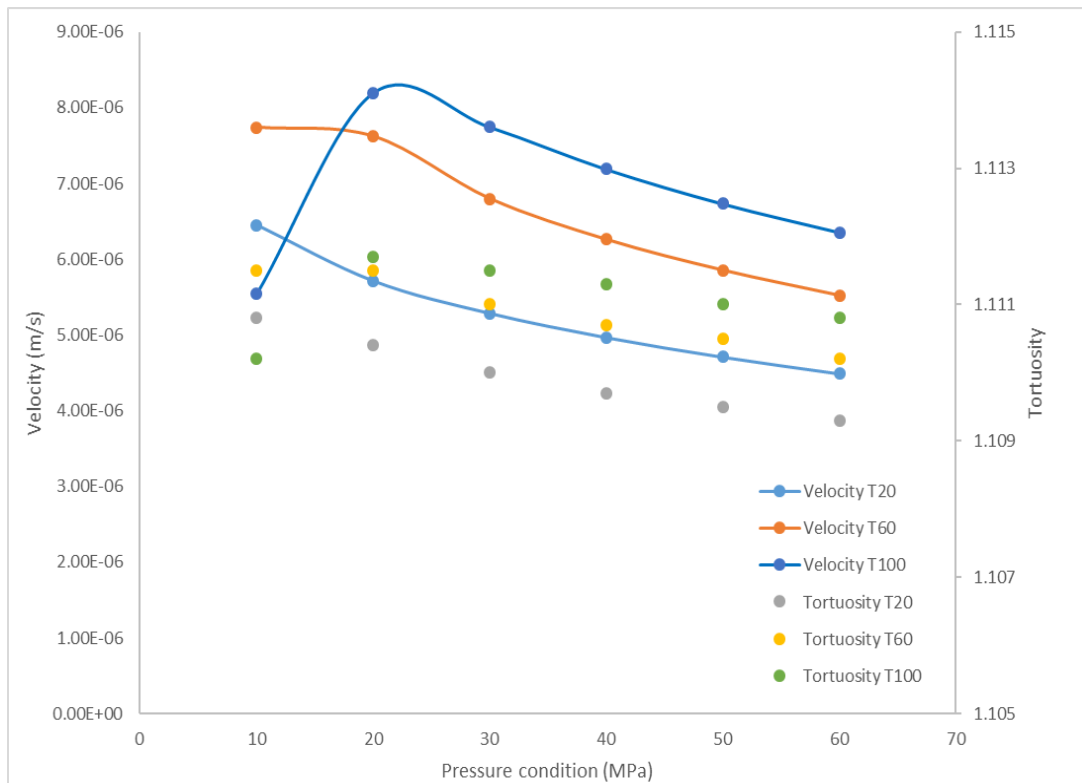
325



326

327

Fig. 11 Velocity and tortuosity for different pressure conditions with $\Delta p = 10$ Pa



328

Fig. 12 Velocity and tortuosity for different pressure conditions with $\Delta p = 0.01$ Pa

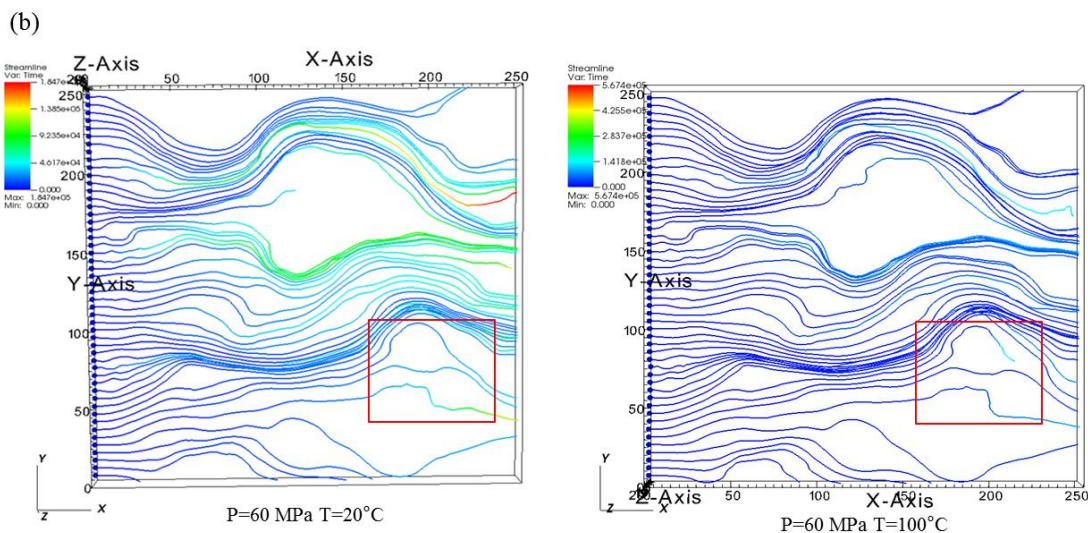
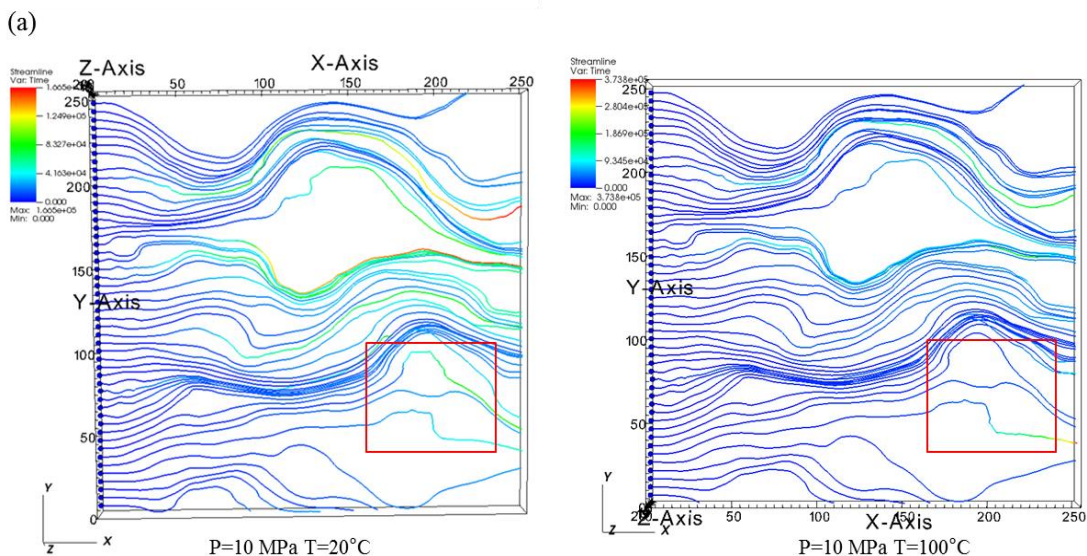


Fig. 13 Streamlines for P=10 and 60 MPa with T=20 and 100°C with $\Delta p = 10$ Pa.

332 For Fig. 14 and 15, the temperature range is from 20°C to 100°C and corresponding pressures
 333 are set as 10, 40 and 60 MPa. The relationships between the average velocity and temperature
 334 in both Fig. 14 and 15 show increasing trends with the increase of temperature for P=40 and
 335 60 MPa, which is because the kinematic viscosities of liquid and supercritical CO₂ in this
 336 temperature range decreases while the temperature becomes larger. The values of the average
 337 velocity equals to about 0.004 m/s with $\Delta p = 10$ Pa and P=40 MPa and the values for P=60
 338 MPa is a little smaller than those of P=40 MPa. Similarly, when $\Delta p = 0.01$ Pa, the velocity
 339 values of P=40 MPa are larger than those of P=60 MPa. And the average velocity for P=10
 340 MPa shows an irregular trend, increasing and then decreasing with the increase of temperature.
 341 As for tortuosity, the curves have almost same trends to the average velocity curves. In addition,
 342 the tortuosity with $\Delta p = 0.01$ Pa is larger compared with tortuosity with $\Delta p = 10$ Pa. Fig. 14
 343 and 15 summarize the liquid and supercritical CO₂ flow for the temperature between 20°C and
 344

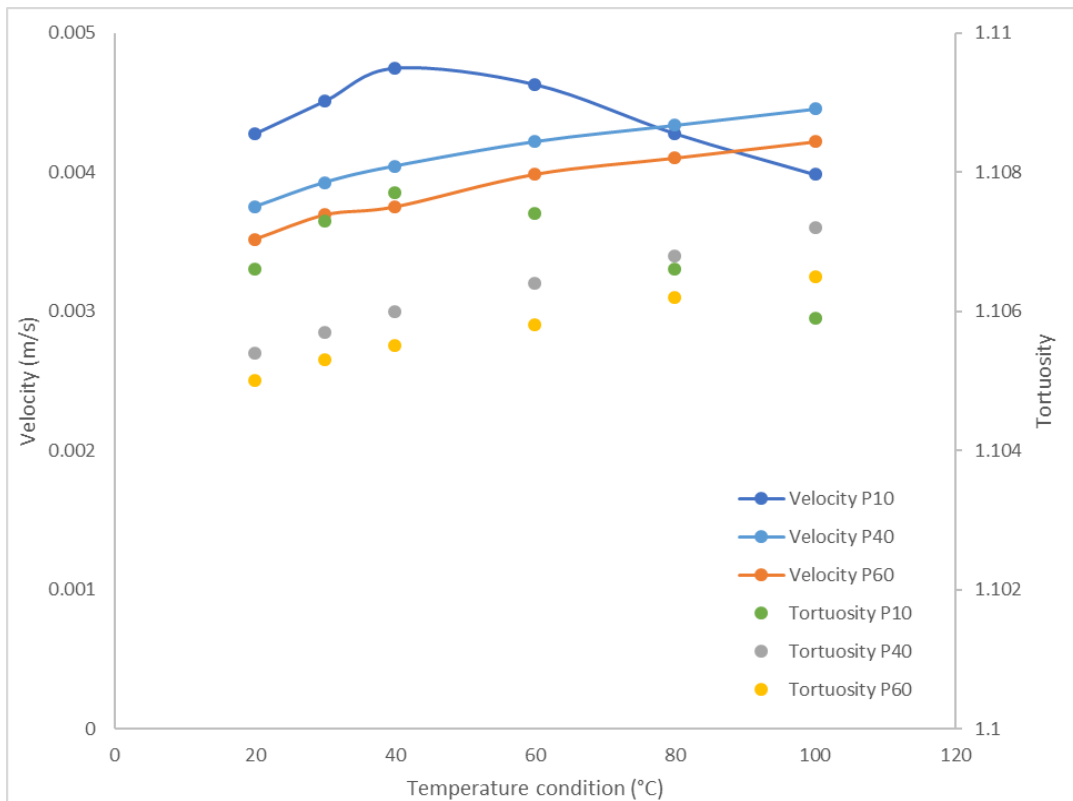
345 100°C in responses to $\Delta p = 10$ and 0.01 Pa respectively under the pressure condition 10, 40
 346 and 60 MPa. It can be concluded that the tortuosity is also tightly related to the temperature.
 347 Fig. 16 gives an illustration of streamlines for T=20 and 100°C with $\Delta p = 0.01$ Pa for two
 348 pressure conditions. It can be seen that the time that streamlines flow through rough fracture
 349 surfaces are different, which also reflect the effects of different temperatures. When
 350 temperature equals to 20°C, the CO₂ stays at liquid state and supercritical CO₂ appears with
 351 the temperature being 100°C. As is stated above, the increase of temperature leads to the
 352 increase of tortuosity. The increases of tortuosity reflected in Fig. 16 shows that the small
 353 proportion of streamlines become more tortuous for P=60 MPa. When pressure equals to 60
 354 MPa, the tortuosity has a positive relationship with the temperature. With the pressure
 355 condition being 10 MPa, the streamlines for T=20 °C are a little more tortuous than the
 356 streamlines for T=100°C because the kinematic viscosity for T=20°C is smaller than that for
 357 T=100°C. From the perspective of quantifying the tortuous behavior, the differences of the
 358 tortuosity values for the pressure condition 10 and 60 MPa equal to 0.0006 and 0.0013
 359 respectively. However, the corresponding differences of tortuosity values are much larger:
 360 0.0029 and 0.0041 (The tortuosity values of the temperature 20°C equal to 1.1899 and 1.1832
 361 and the tortuosity values of the temperature 100°C are 1.1928 and 1.1791), as is shown in Table.
 362 2.

363 Table. 1 Comparisons of tortuosity differences between the surrounded and whole areas at
 364 different temperature conditions

	Tortuosity of T=20°C	Tortuosity of T=100°C	Tortuosity differences in the surrounded area	Tortuosity differences of the whole area
P=10 MPa	1.1899	1.1928	0.0029	0.0006
P=60 MPa	1.1832	1.1791	0.0041	0.0013

365 In addition, it can be found that the average velocity and tortuosity curves for the pressure
 366 condition P=40 MPa are both located higher than those for P=60 MPa in Fig. 14 and 15.
 367 Similarly, the average velocity and tortuosity curves for the temperature T= 60°C are higher
 368 than those for T=20°C. To summarize, the results shown in Fig. 14 and 15 and the results from
 369 Fig. 11 and 12 provide mutual validations.

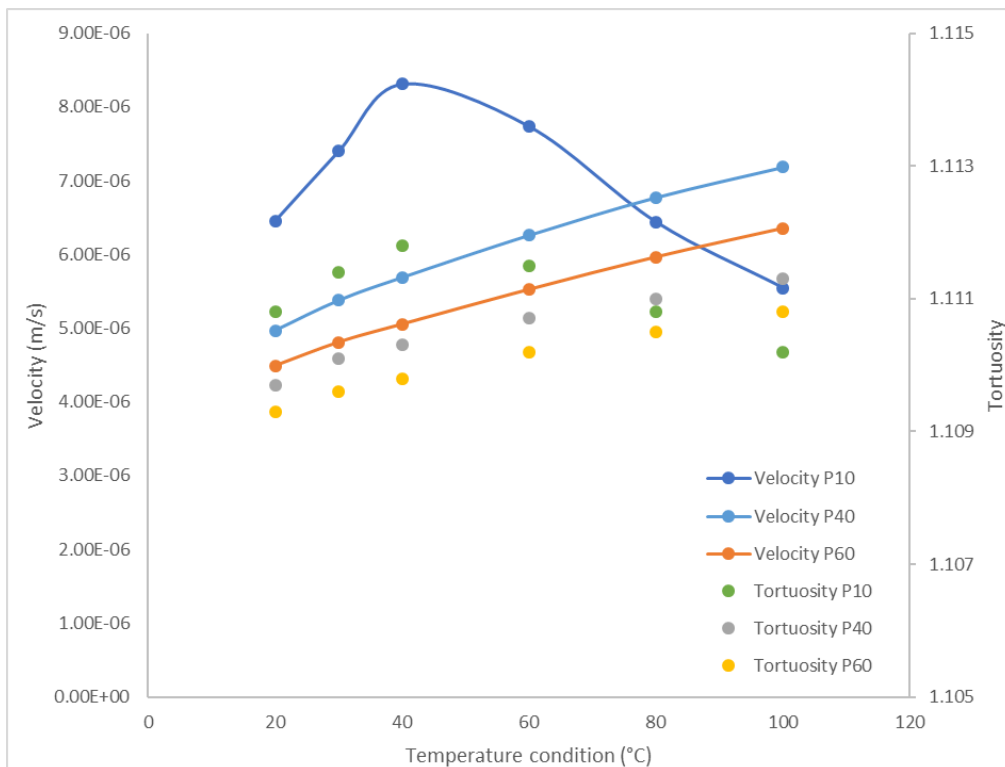
370



371

372

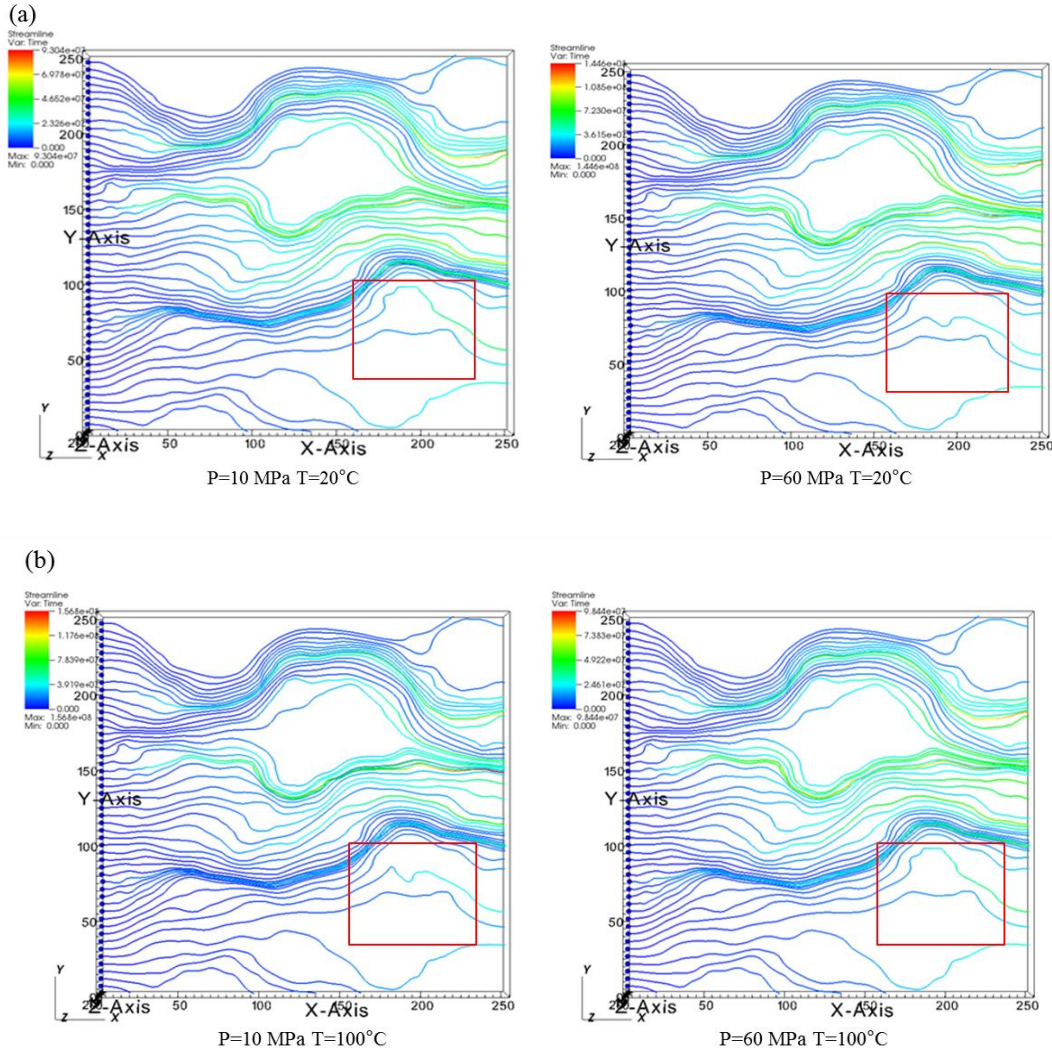
Fig.14 Velocity and tortuosity for different temperature conditions with $\Delta p = 10$ Pa



373

374

Fig. 15 Velocity and tortuosity for different temperature conditions with $\Delta p = 0.01$ Pa



375

376

377

Fig. 16 Streamlines for $T=20$ and 100°C with $P=10$ and 60 MPa and $\Delta p = 0.01$ Pa

378

379

380

381

382

383

384

385

386

387

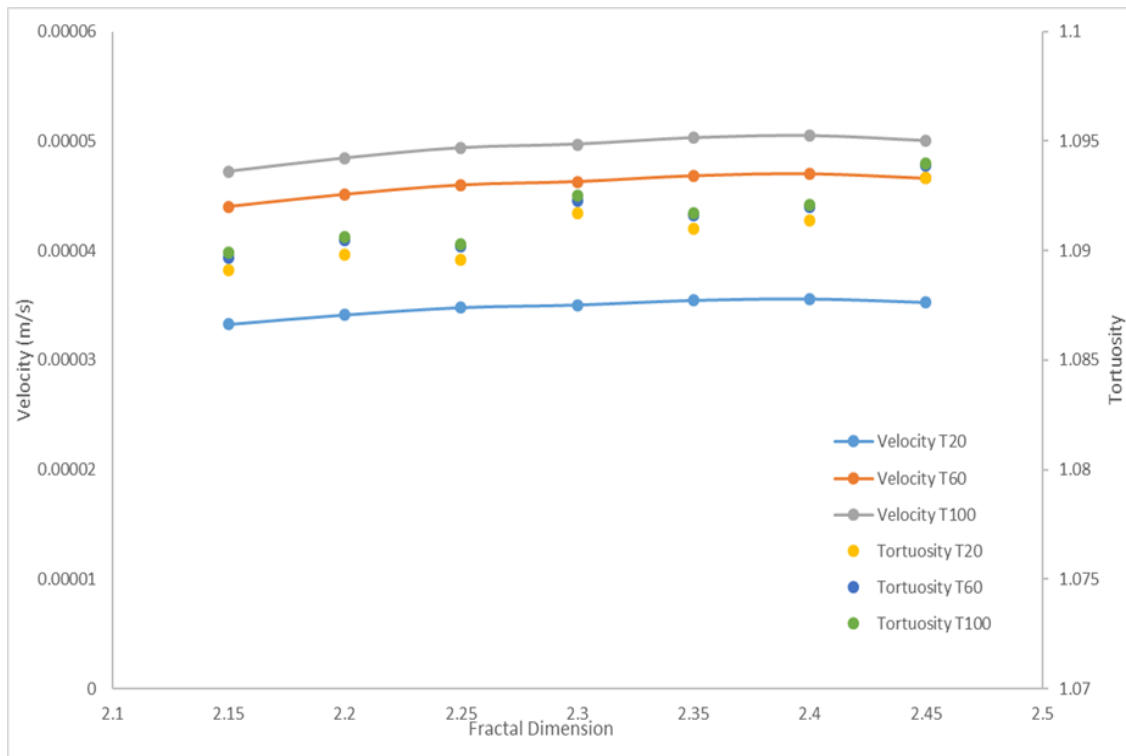
388

389

390

391

In addition to the grid resolution validation, the validations of fracture surface roughness (geometry) and scales of the fracture model size are also needed for consideration. A fracture model with its size being 6.4×6.4 mm is used here. Similarly, the X-Y plane is divided into 128×128 grids. Fig. 17 shows the average velocity and tortuosity curves changes with the increase of the fractal dimension that is used to generate corresponding fracture surface roughness for different temperatures (20 , 60 and 100°C) under the same pressure condition $P=20$ MPa. The values of the fractal dimension are from 2.15 to 2.45 with the interval being 0.05 . It can be found that the differences among the values of the average velocity and tortuosity for different temperatures are almost same with corresponding to different fractal dimensions, which validate results shown in above figures. Furthermore, the velocity and tortuosity correlations don't show similar trends with the increasing fractal dimensions, which is different from Fig. 11, 12, 14 and 15. This reflects that the average velocity and tortuosity curves have similar trends due to the CO_2 density determined by the pressure and temperature conditions, not affected by the fracture surface roughness (geometry).



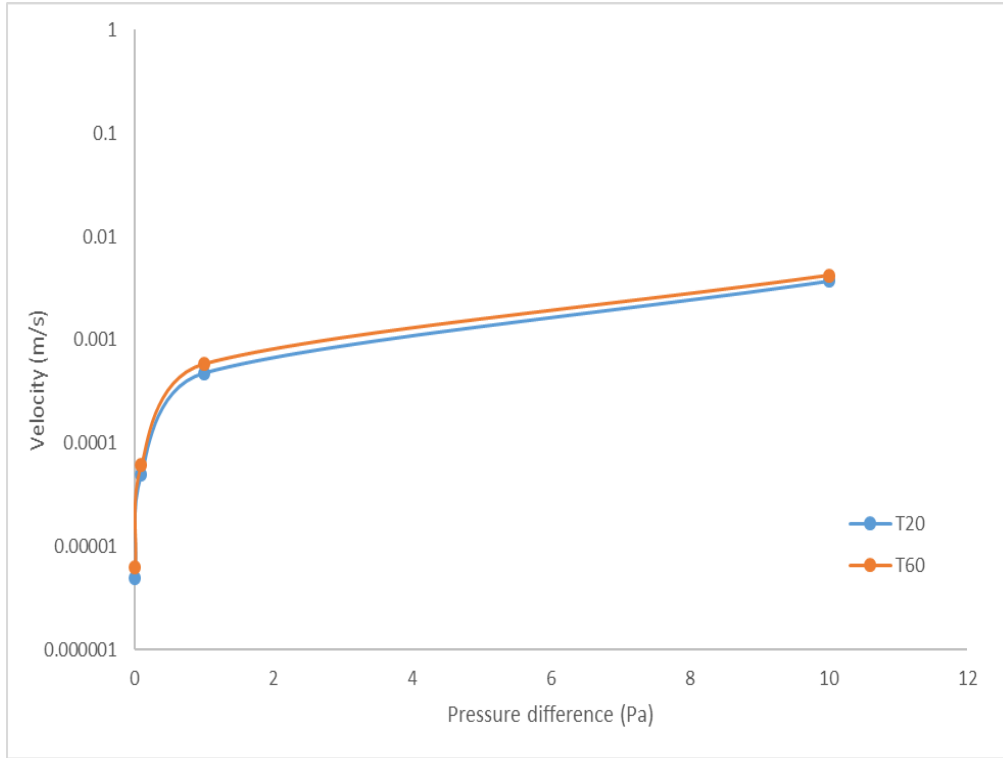
392
 393 Fig. 17 Velocity and tortuosity for different fractal dimensions with the pressure condition 20
 394 MPa

395 In Fig. 18, two semi-log curves for different values of the pressure difference Δp with the
 396 temperature $T=20$ and 60°C under the condition of $P=40$ MPa is shown. The values of Δp
 397 include: 10, 1, 0.1 and 0.01 Pa. The semi-log curves are adopted in order to have a better
 398 identification for the differences of velocities among Δp values. The average velocity values
 399 for $T=60^\circ\text{C}$ are larger than those for $T=20^\circ\text{C}$ because the kinematic viscosity for $T=60^\circ\text{C}$ is
 400 smaller than that for $T=20^\circ\text{C}$. And the average velocity values increase with the pressure
 401 difference becoming larger. Fig. 19 shows that the tortuosity become smaller with the increase
 402 of the pressure difference. And the values of tortuosity varies around 1.115. And the tortuosity
 403 for $T=60^\circ\text{C}$ is larger than the tortuosity for $T=20^\circ\text{C}$. This is because the kinematic viscosity for
 404 $T=60^\circ\text{C}$ is smaller than that for $T=20^\circ\text{C}$ when the pressure equals to 40 MPa.

405 Fig. 20 and 21 show the differences of streamlines corresponding to four pressure differences
 406 for the temperature $T=20$ and 60°C respectively, playing a complementary role in
 407 demonstrating the changes of tortuosity in Fig. 18 and 19. In both Fig. 20 and 21, there are
 408 differences in streamlines that can be observed to certain extent. The streamlines surrounded
 409 by red borders are almost the same in both Fig. 20 and 21, which are reflected in the calculation
 410 results of tortuosity differences. The tortuosity differences of the whole fracture between the
 411 pressure difference 10 and 0.01 Pa for the temperature 20 and 60°C both equal to 0.0043,
 412 which are similar to the tortuosity differences of the surrounded area (0.0057 and 0.0063). In
 413 addition, the streamlines in the area surrounded by the red border are easy to be seen the extent
 414 of concentrations from 10 to 0.01 Pa. At these cases, with the temperature and pressure
 415 conditions remaining constant, various velocities that are determined by Δp result in different
 416 streamlines. When the average velocity increases by scales in these cases, the streamlines

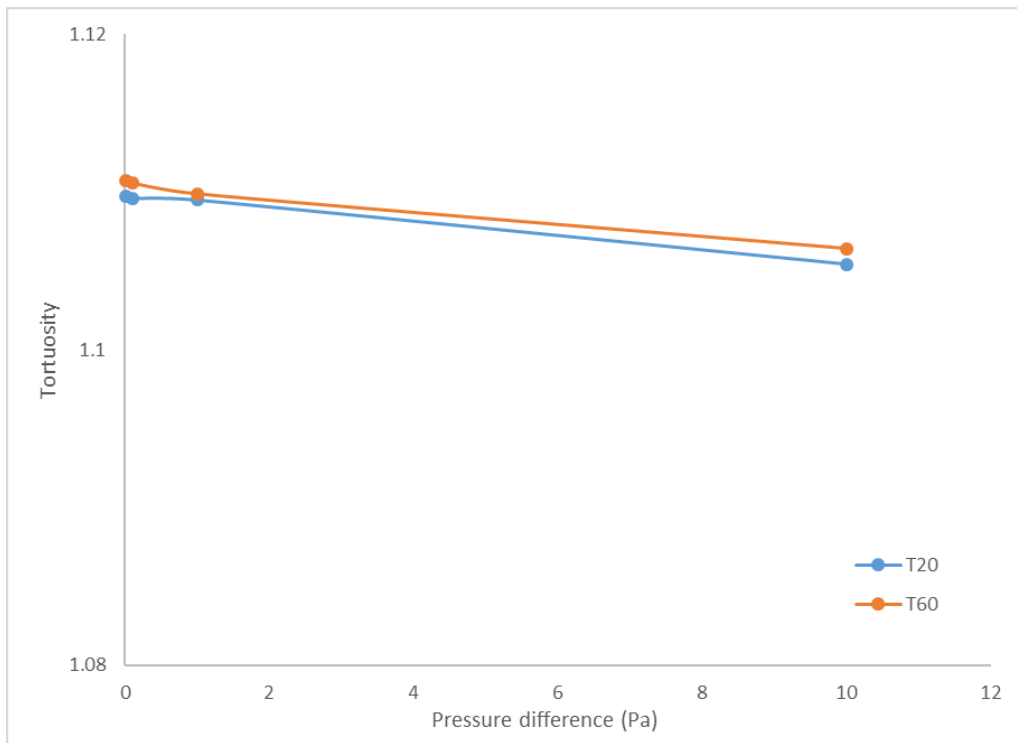
417 become more concentrated. As a result, the tortuosity decreases with the upscale of the average
418 velocity.

419 Fig. 18, 19, 20 and 21 give detailed illustrations that the tortuosity becomes smaller and
420 streamlines become more concentrated due to the upscaling velocity that is caused by different
421 sets of the pressure difference with combination of the streamline distributions, which is also
422 validated by the above results.



423

424 Fig. 18 Semi-log relationships between velocity and Δp for different temperature conditions
425 with P=40 MPa

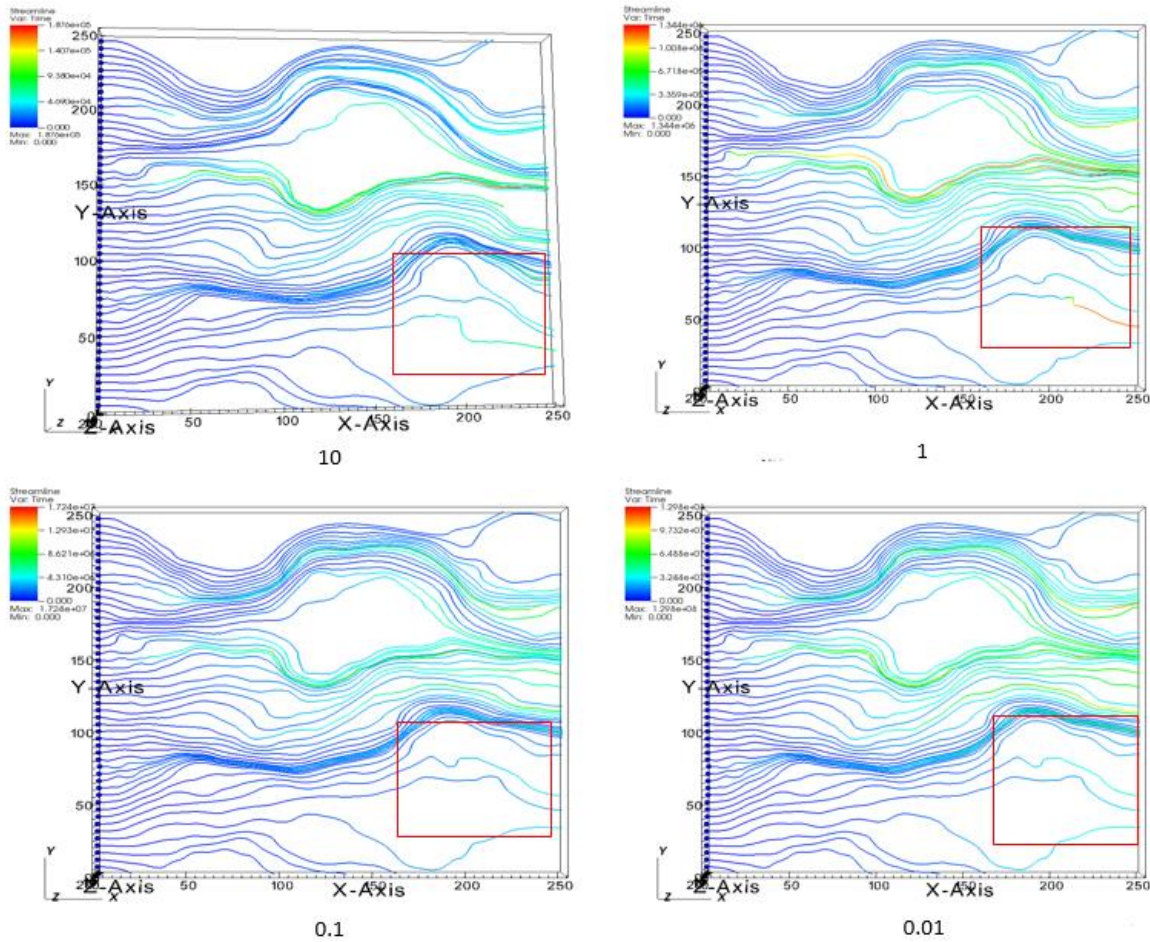


426

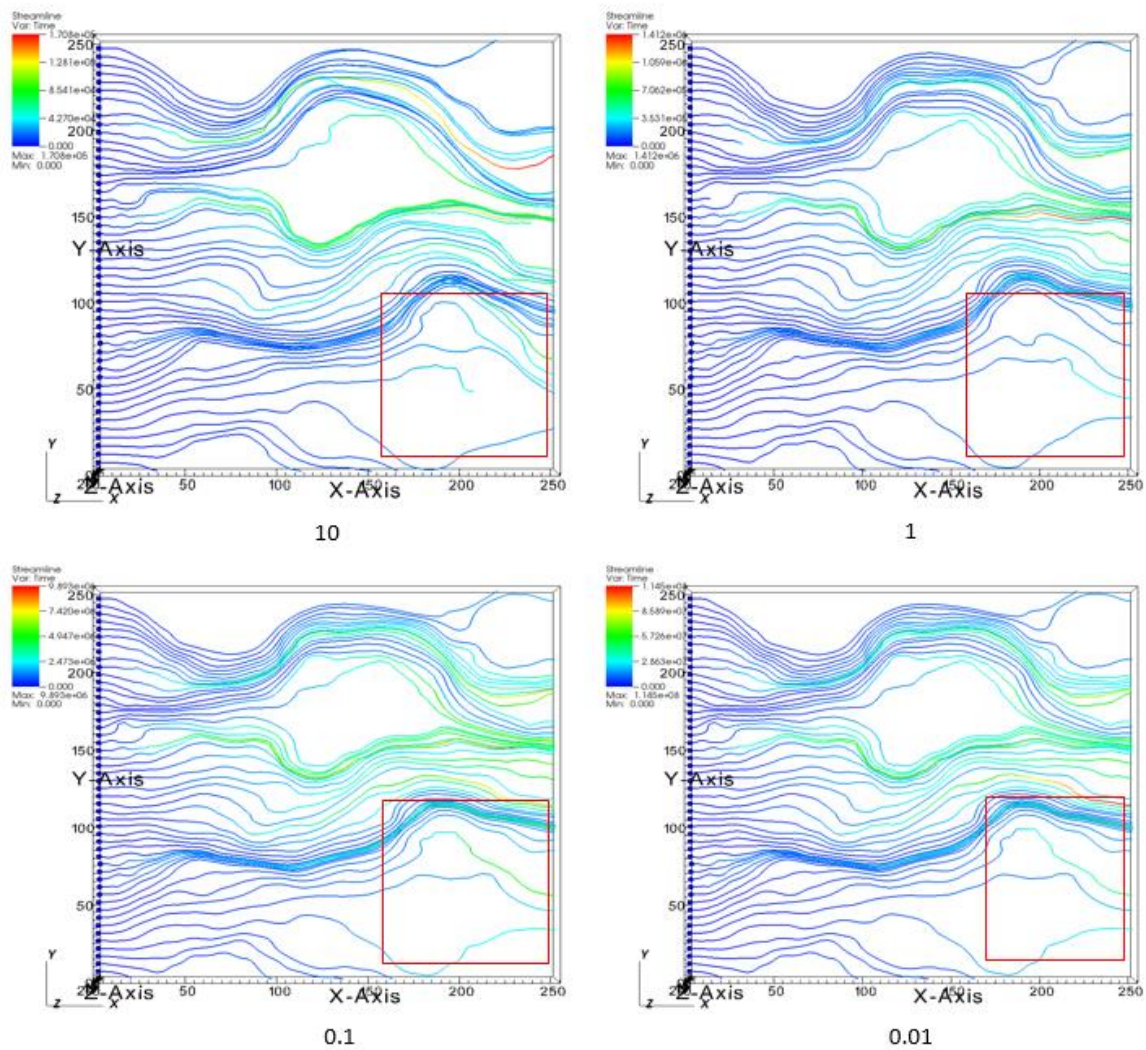
427 Fig. 19 The relationship between tortuosity and Δp for different temperature conditions with

428

P=40 MPa



429

Fig. 20 Streamlines for different Δp with P=40 MPa and T=20°C

431

432

Fig. 21 Streamlines for different Δp with P=40 MPa and T=60°C

433 Conclusions

434 It is the first time to investigate the effects of liquid and supercritical CO₂ properties on flow
 435 behaviors through a single 3D self-affine rough fracture by using the Lattice Boltzmann method.
 436 A D3Q19 LBM code has been programmed to generate the numerical fracture model that gives
 437 an accurate reflection of fracture surface roughness and to simulate the liquid and supercritical
 438 CO₂ flow under various pressure and temperature conditions with certain pressure differences
 439 between injecting and discharging surfaces. The different properties of liquid and supercritical
 440 CO₂ were calculated by Peng-Robinson Equation of State through changing relevant pressures
 441 and temperatures. Different CO₂ properties were used to generate corresponding average
 442 velocity and tortuosity curves and was used to generate the velocity and streamlines
 443 distributions under various pressure differences. The streamlines distributions show an
 444 irregular pattern due to the rough fracture surfaces and play a significant role in analysing
 445 relevant tortuosity changes. It was found that the average velocity and tortuosity have tight
 446 relationships with temperature and pressure conditions while other conditions keep constant,
 447 which were validated mutually. The streamlines tend to be more tortuous with the gradual

448 increase of the kinematic viscosity when average velocities are similar at the same scale. The
449 tortuosity decreases with the upscaling of average velocity. With upscaling the average velocity,
450 the streamlines become more concentrated for the same CO₂ properties. In addition, it has been
451 proven that the similar trends of the average velocity and tortuosity curves are not affected by
452 the fracture surface roughness. This paper provides an efficient and accurate evaluation of the
453 effects of CO₂ properties on flow behaviors at low velocities through a rough fracture, which
454 has a great significance in the natural and induced fracture reservoirs for the purposes of CO₂
455 storage, enhanced shale gas/oil recovery and enhanced geothermal systems.

456 **Nomenclature**

457	C	the characteristic lattice velocity in a cell size
458	e_i	velocity in the i -th direction in a LBM cell
459	D_f	fractal dimension
460	H	Hurst exponent
461	L	Characteristic length
462	r	a constant value
463	t	time
464	P	pressure
465	T	temperature
466	V	velocity magnitude
467	u	velocity in LBM
468	X, Y, Z	directions

469 **Greek Symbols**

470	ρ	density
471	σ	standards deviation
472	τ	the relaxation time
473	μ	the dynamic viscosity
474	ν	the kinematic viscosity
475	Ω_{col}	the collision operator
476	ω_i	the weight factor in the i -th direction
477	δ_x	the length of each grid
478	δ_t	the length of time step

479 **References**

- 480 [1] Grimston MC, Karakoussis V, Fouquet R, van der Vorst R, Pearson P, Leach M. The
481 European and global potential of carbon dioxide sequestration in tackling climate change.
482 Climate Policy 2001; 1(2): 155-71.
- 483 [2] Li ZW, Dong MZ, Li SL, Huang S. CO₂ sequestration in depleted oil and gas reservoirs—
484 caprock characterization and storage capacity. Energy conversion and management 2006;
485 47(11-12): 1372-82.

- 486 [3] Global CCS Institute. Introduction to carbon capture and storage. Global Status of CCS
487 2016: Special Report.
- 488 [4] Milan JP, Eric FM, Michael LJ. High-fidelity reservoir simulations of enhanced gas
489 recovery with supercritical CO₂. *Energy* 2016: 111: 548-59.
- 490 [5] Sun XH, Wang ZY, Sun BJ, Wang WD. Research on hydrate formation rules in the
491 formations for liquid CO₂ fracturing. *Journal of Natural Gas Science and Engineering*
492 2016: 33: 1390-1401.
- 493 [6] Brown DW. A hot dry rock geothermal energy concept utilizing supercritical CO₂ instead
494 of water. In: *Proceedings of the Twenty-Fifth Workshop on Geothermal Reservoir*
495 *Engineering*, Stanford University, CA, January 24-26, 2000, SGP-TR-165.
- 496 [7] Fouillac C, Sanjuan B, Gentier S, Czernichowski-Lauriol I. Could sequestration of CO₂
497 be combined with the development of Enhanced Geothermal Systems? In: *Third Annual*
498 *Conference on Carbon Capture and Sequestration*, Alexandria, VA, May 3-6, 2004.
- 499 [8] Pruess K. Enhanced geothermal systems (EGS) using CO₂ as working fluid – a novel
500 approach for generating renewable energy with simultaneous sequestration of carbon.
501 *Geothermics* 2006: 35: 351–67.
- 502 [9] Wang F, Fu SF, Guo G, Jia ZZ, Luo SJ, Guo RB. Experimental study on hydrate-based
503 CO₂ removal from CH₄/CO₂ mixture. *Energy* 2016: 104: 76-84.
- 504 [10] Liu YG, Hou J, Zhao HF, Liu XY, Xia ZZ. A method to recover natural gas hydrates with
505 geothermal energy conveyed by CO₂. *Energy* 2018: 144: 265-78.
- 506 [11] Alvarado V, Manrique E. Enhanced Oil Recovery: An Update Review. *Energies* 2010:
507 3:1529-75.
- 508 [12] Shukla R, Ranjith P, Haque A, Choi X. A review of studies on CO₂ sequestration and
509 caprock integrity. *Fuel* 2010: 89(10): 2651-64.
- 510 [13] Xu RN, Zhang L, Zhang FZ, Jiang PX. A Review on heat transfer and energy conversion
511 in the enhanced geothermal systems with water/CO₂ as working fluid. *International*
512 *Journal of Energy Research* 2015: 39(13): 1722-41.
- 513 [14] Tudor R, Vozniak C, Peters W, Banks ML. Technical advances in liquid CO₂ fracturing.
514 In: *Annual Technical Meeting*, June 12 - 15, 1994, Calgary, Alberta. PETSOC-94-36.
- 515 [15] Michael GT, Richard EM. A comparison of results of three different CO₂ energized frac
516 fluids: a case history. In: *SPE Gas Technology Symposium*, April 30-May 2, 2002,
517 Calgary, Alberta, Canada. SPE-75681-MS.
- 518 [16] Lu M, Connell LD. The transient behavior of CO₂ flow with phase transition in injection
519 wells during geological storage - Application to a case study. *Journal of Petroleum Science*
520 *Engineering* 2014: 124: 7–18.
- 521 [17] Zhang XW, Lu YY, Tang JR, Zhou Z, Liao Y. Experimental study on fracture initiation
522 and propagation in shale using supercritical carbon dioxide fracturing. *Fuel* 2017: 190:
523 370-378.
- 524 [18] Ishida T, Chen YQ, Bennour Z, Yamashita H, Inui S, Nagaya Y, Naoi M, Chen Q,
525 Nakayama Y, Nagano Y. Features of CO₂ fracturing deduced from acoustic emission and
526 microscopy in laboratory experiments. *Journal of Geophysical Research: Solid Earth*:
527 121(11): 8080-98.

- 528 [19] Zhang L, Jiang PX, Wang ZC, Xu RN. Convective heat transfer of supercritical CO₂ in a
529 rock fracture for enhanced geothermal systems. *Applied Thermal Engineering* 2017: 115:
530 923-36.
- 531 [20] Meier P, Ivory J, Rocco M, Scott K. Field and laboratory measurements of leakoff
532 parameters for liquid CO₂ and liquid CO₂/N₂ fracturing. In: Annual Technical Meeting, June
533 8 - 11, 1997, Calgary, Alberta. PETSOC-97-105.
- 534 [21] Zou YS, Li N, Ma XF, Zhang SC, Li SH. Experimental study on the growth behavior of
535 supercritical CO₂-induced fractures in a layered tight sandstone formation. *Journal of*
536 *Natural Gas Science and Engineering* 2018: 49: 145-56.
- 537 [22] Zhou X, Burbey TJ. Fluid effect on hydraulic fracture propagation behavior: a comparison
538 between water and supercritical CO₂-like fluid. *Geofluids* 2014: 14(2): 174-88.
- 539 [23] Borgia A, Oldenburg CM, Zhang R, Pan LH, Daley TM, Finsterle S, Ramakrishnan TS.
540 Simulations of CO₂ injection into fractures and faults for improving their geophysical
541 characterization at EGS sites. *Geothermics* 2017: 69: 189-201.
- 542 [24] Wang JT, Sun BJ, Li H, Wang X, Wang ZY, Sun XH. Phase state control model of
543 supercritical CO₂ fracturing by temperature control. *International Journal of Heat and*
544 *Mass Transfer* 2018: 118: 1012-21.
- 545 [25] Lomize GM. Flow in fractured rocks (in Russian). Gesemergoizdat, Moscow, Russia,
546 1951.
- 547 [26] Gangi AF. Variation of whole and fractured porous rock permeability with confining
548 pressure. *International Journal of Rock Mechanics and Mining Sciences & Geomechanics*
549 *Abstracts* 1978: 15(5): 249-257.
- 550 [27] Berkowitz B, Braester C. Solute transport in fracture channel and parallel plate models.
551 *Geophysical Research Letters* 1991: 18(2): 227-30.
- 552 [28] Liu ZY, Chen M, Zhang GQ. Analysis of the influence of a natural fracture network on
553 hydraulic fracture propagation in carbonate formations. *Rock Mechanics and Rock*
554 *Engineering* 2014: 47(2): 575-87.
- 555 [29] Lanaro F. A random field model for surface roughness and aperture of rock fractures.
556 *International Journal of Rock Mechanics and Mining Sciences* 2000: 37(8): 1195–1210.
- 557 [30] Gouze P, Noiriél C, Bruderer C, Loggia D, Leprovost R. X-ray tomography
558 characterization of fracture surfaces during dissolution. *Geophysical Research Letters*
559 2003: 30(5): 1267.
- 560 [31] Muralidharan V, Chakravarthy D, Putra E, Schechter DS. Investigating fracture aperture
561 distributions under various stress conditions using X-Ray CT scanner. In: Canadian
562 International Petroleum Conference, June 8-10, 2004, Calgary, Alberta, Canada.
563 PETSOC-2004-230.
- 564 [32] Qian J, Zhan H, Zhao W, Sun F. Experimental study of turbulent unconfined groundwater
565 flow in a single fracture. *Journal of Hydrology* 2005: 311(1-4): 134-42.
- 566 [33] Qian J, Chen Z, Zhan H, Guan H. Experimental study of the effect of roughness and
567 Reynolds number on fluid flow in rough-walled single fractures: a check of local cubic
568 law. *Hydrological Processes* 2011: 25(4): 614-622.
- 569 [34] Su GW, Geller JT, Pruess K, Wen F. Experimental studies of water seepage and
570 intermittent flow in unsaturated, rough-walled fractures. *Water Resources Research* 1999:
571 35(4):1019-37.

- 572 [35] Noiriél C, Gouze P, Made B. 3D analysis of geometry and flow changes in a limestone
573 fracture during dissolution. *Journal of Hydrology* 2013;486: 211-23.
- 574 [36] Tsang CF, Neretnieks I. Flow channeling in heterogeneous fractured rocks. *Reviews of*
575 *Geophysics* 1998: 36(2): 275-298.
- 576 [37] Co CKD, Pollard DD, Horne RN. Towards a better understanding of the impact of fracture
577 roughness on permeability-stress relationships using first principles. 2017 42nd Stanford
578 Geothermal Workshop Proceedings.
- 579 [38] Hakami E, Larsson E. Aperture measurements and flow experiments on a single natural
580 fracture. *International J Rock Mechanics and Mining Science* 1996: 33(4): 395-404.
- 581 [39] Channeling experiment. Technical report, Swedish Nuclear Fuel and Waste Management
582 Company, 1990.
- 583 [40] Watanabe N, Hirano N, Tsuchiya N. Determination of aperture structure and fluid flow in
584 a rock fracture by high-resolution numerical modelling on the basis of a flow-through
585 experiment under confining pressure. *Water Resources Research* 2008: 44(6): W06412.
- 586 [41] Brown SR. Fluid flow through rock joints the effect of surface roughness. *Journal of*
587 *Geophysical Research* 1987: 92 (B2): 1337-1347.
- 588 [42] Zimmerman RW, Kumar S, Bodvarsson GS. Lubrication theory analysis of the
589 permeability of rough-walled fractures. *International Journal of Rock Mechanics and*
590 *Mining Sciences & Geomechanics Abstracts* 1991: 28(4): 325-31.
- 591 [43] Brush DJ, Thomson NR. Fluid flow in synthetic rough-walled fractures: Navier-Stokes,
592 Stokes, and local cubic law simulations. *Water Resource Research* 2003: 39(4): 1085.
- 593 [44] Yeo IW, Ge S. Applicable range of the Reynolds equation for fluid flow in a rock Fracture.
594 *Geosciences Journal* 2005: 9 (4): 347-52.
- 595 [45] Ishibashi T, Watanabe N, Hirano N, Okamoto A, Tsuchiya N. Upgrading of aperture model
596 based on surface geometry of natural fracture for evaluating channeling flow. *GRC*
597 *Transactions* 2012: 36: 481- 86.
- 598 [46] Wang L, Cardenas MB, Slottke DT, Ketcham RA, Sharp JM. Modification of the Local
599 Cubic Law of fracture flow for weak inertia, tortuosity, and roughness. *Water Resources*
600 *Research* 2015: 51(4): 2064-80.
- 601 [47] Kim J, Gao X, Srivatsan TS. Modeling of crack growth in ductile solids: a three-
602 dimensional analysis. *International Journal of Solids and Structures* 2003: 40: 7357-74.
- 603 [48] Tan YF, Zhou ZF. Simulation of solute transport in a parallel single fracture with
604 LBM/MMP mixed method. *Journal of Hydrodynamics* 2008: 20(3): 365-72.
- 605 [49] Eker E, Akin S. Lattice Boltzmann simulation of fluid flow in synthetic fractures.
606 *Transport in Porous Media* 2006: 65(3): 363-84.
- 607 [50] Dou Z, Zhou Z, Sleep BE. Influence of wettability on interfacial area during immiscible
608 liquid invasion into a 3D self-affine rough fracture: Lattice Boltzmann simulations.
609 *Advances in Water Resources* 2013: 61: 1-11.
- 610 [51] Wang M, Chen Y, Ma G, Zhou J, Zhou C. Influence of surface roughness on nonlinear
611 flow behaviors in 3D self-affine rough fractures: Lattice Boltzmann simulations.
612 *Advances in Water Resources* 2016: 96: 373-88.
- 613 [52] Briggs S, Karney BW, Sleep BE. Numerical modeling of the effects of roughness on flow
614 and eddy formation in fractures. *Journal of Rock Mechanics and Geotechnical*
615 *Engineering* 2017: 9: 105-15.

- 616 [53] Li JW, Claudi C, Sergio GT, Li Z, Li L. Laboratory investigation of flow paths in 3D self-
617 affine fractures with Lattice Boltzmann simulations. *Energies* 2018; 11(1): 168.
- 618 [54] Neuville A, Toussaint R, Schmittbuhl J. Fracture roughness and thermal exchange: A case
619 study at Soultz-sous-Forêts. *Comptes Rendus Geoscience* 2010; 342(78): 616 -625.
- 620 [55] He Y, Bai B, Hu S, Li X. Effects of surface roughness on the heat transfer characteristics
621 of water flow through a single granite fracture. *Computers and Geotechnics* 2016; 80: 312-
622 21.
- 623 [56] Luo S, Zhao Z, Peng H, Pu H. The role of fracture surface roughness in macroscopic fluid
624 flow and heat transfer in fractured rocks. *International Journal of Rock Mechanics and*
625 *Mining Sciences* 2016; 87: 29-38.
- 626 [57] Fox DB, Koch DL, Tester JW. The effect of spatial aperture variations on the thermal
627 performance of discretely fractured geothermal reservoirs. *Geothermal Energy* 2015; 3:
628 21.
- 629 [58] Huang SL, Oelfke SM, Speke RC. Applicability of fractal characterization and modelling
630 to rock joint profiles. *International Journal of Rock Mechanics and Mining Sciences &*
631 *Geomechanics Abstracts* 1992; 29(2): 89-98.
- 632 [59] Odling NE. Natural fracture profiles, fractal dimension and joint roughness coefficients.
633 *Rock Mechanics and Rock Engineering* 1994; 27(3): 135-53.
- 634 [60] Schmittbuhl J, Steyer A, Jouniaux L, Toussaint R. Fracture morphology and viscous
635 transport. *International Journal of Rock Mechanics and Mining Sciences* 2008; 45(3):
636 422–430.
- 637 [61] Mandelbrot BB. *The fractal geometry of nature*. Freeman 1982, San Francisco.
- 638 [62] Mandelbrot BB. Self-affine fractals and fractal dimension. *Physical Scripta* 1985; 32: 257-
639 60.
- 640 [63] Molz F, Liu H, Szulga J. Fractional Brownian motion and fractional Gaussian noise in
641 subsurface hydrology: a review, presentation of fundamental properties, and extensions.
642 *Water Resource Research* 1997; 33(10): 2273–86.
- 643 [64] Babadagli T, Ren X, Develi K. Effects of fractal surface roughness and lithology on single
644 and multiphase flow in a single fracture: An experimental investigation. *International*
645 *Journal of Multiphase Flow* 2015; 68: 40-58.
- 646 [65] Power WL, Tullis TE, Brown SR, Boitnott GN, Scholz CH. Roughness of natural fault
647 surfaces. *Geophysical Research Letter* 1987; 14 (1): 29-32.
- 648 [66] Ogilvie SR, Isakov E, Glover PWJ. Fluid flow through rough fractures in rocks. II: A new
649 matching model for rough rock fractures. *Earth and Planetary Science Letters* 2006:
650 241(3–4): 454–65.
- 651 [67] Succi S. *The Lattice Boltzmann Equation for fluid dynamics and beyond*. 2001, Clarendon
652 Press, Oxford University.
- 653 [68] Qian YH, d’Humières D, Lallemand P. Lattice BGK models for Navier-Stokes equation.
654 *Europhysical Letter* 1992; 17(6): 479.
- 655 [69] Okabe H, Blunt MJ. Prediction of permeability for porous media reconstructed using
656 multiple-point statistics. *Physical Review E* 2004; 70: 066135.
- 657 [70] Shi XY, Gao H, Lazouskaya VI, Kang Q, Jin Y, Wang LP. Viscous flow and colloid
658 transport near air-water interface in a microchannel. *Computers & Mathematics with*
659 *Applications* 2010; 59: 2290-2304.

660 [71] Li Q, Luo KH, Kang QJ, He YL, Chen Q, Liu Q. Lattice Boltzmann methods for
661 multiphase flow and phase-change heat transfer. *Progress in Energy and Combustion*
662 *Science* 2016; 52: 62-105.

663 [72] He X, Luo LS. Lattice Boltzmann model for the incompressible Navier-Stokes equation.
664 *Journal of Statistical Physics* 1997; 88(3-4):927-44.

665 [73] Mohamad AA. *Lattice Boltzmann Method: Fundamentals and Engineering Applications*
666 *with Computer Codes*. Springer-Verlag 2011, London.

667 [74] Huang H, Sukop M, Lu X. *Multiphase lattice Boltzmann methods: Theory and application*.
668 John Wiley & Sons, 2015.

669 [75] Duda A, Koza Z, Matyka M. Hydraulic tortuosity in arbitrary porous media flow. *Physical*
670 *Review E* 2011; 84: 036319.

671 [76] Sheikh B, Pak A. Numerical investigation of the effects of porosity and tortuosity on soil
672 permeability using coupled three-dimensional discrete-element method and lattice
673 Boltzmann method. *Physical Review E* 2015; 91: 053301.

674

675

676

677

678

679

680